

Non-Gaussianity in the Very Small Array CMB maps with Smooth-Goodness-of-fit tests

José Alberto Rubiño-Martín^{1*}, Antonio M. Aliaga², R. B. Barreiro²,
 Richard A. Battye³, Pedro Carreira³, Kieran Cleary^{3†}, Rod D. Davies³,
 Richard J. Davis³, Clive Dickinson^{3‡}, Ricardo Génova-Santos¹, Keith Grainge⁴,
 Carlos M. Gutiérrez¹, Yaser A. Hafez³, Michael P. Hobson⁴, Michael E. Jones^{4§},
 Rüdiger Kneissl⁴, Katy Lancaster⁴, Anthony Lasenby⁴, J. P. Leahy³, Klaus Maisinger⁴,
 Enrique Martínez-González², Guy G. Pooley⁴, Nutan Rajguru⁴, Rafael Rebolo^{1,5},
 José Luis Sanz², Richard D.E. Saunders⁴, Richard S. Savage^{4¶}, Anna Scaife⁴,
 Paul Scott⁴, Anže Slosar^{4||}, Angela C. Taylor^{4**}, David Titterton⁴,
 Elizabeth Waldram⁴, Robert A. Watson^{3††}

¹*Instituto de Astrofísica de Canarias, 38200 La Laguna, Tenerife, Spain.*

²*IFCA, CSIC-Univ. de Cantabria, Avda. los Castros, s/n, E-39005 Santander, Spain*

³*University of Manchester, Jodrell Bank Observatory, UK.*

⁴*Astrophysics Group, Cavendish Laboratory, University of Cambridge, UK.*

⁵*Consejo Superior de Investigaciones Científicas, Spain.*

Accepted Received In original form

ABSTRACT

We have used the Rayner & Best (1989) smooth tests of goodness-of-fit to study the Gaussianity of the Very Small Array (VSA) data. These tests are designed to be sensitive to the presence of ‘smooth’ deviations from a given distribution, and are applied to the data transformed into normalised signal-to-noise eigenmodes. In a previous work, they have been already adapted and applied to simulated observations of interferometric experiments. In this paper, we extend the practical implementation of the method to deal with mosaiced observations, by introducing the Arnoldi algorithm. This method permits us to solve large eigenvalue problems with low computational cost.

Out of the 41 published VSA individual pointings dedicated to cosmological (CMB) observations, 37 are found to be consistent with Gaussianity, whereas four pointings show deviations from Gaussianity. In two of them, these deviations can be explained as residual systematic effects of a few visibility points which, when corrected, have a negligible impact on the angular power spectrum. The non-Gaussianity found in the other two (adjacent) pointings seems to be associated to a local deviation of the power spectrum of these fields with respect to the common power spectrum of the complete data set, at angular scales of the third acoustic peak ($\ell = 700 - 900$). No evidence of residual systematics is found in this case, and unsubtracted point sources are not a plausible explanation either. If those visibilities are removed, the differences of the new power spectrum with respect to the published one only affect three bins. A cosmological analysis based on this new VSA power spectrum alone shows no differences in the parameter constraints with respect to our published results, except for the physical baryon density, which decreases by 10 percent.

Finally, the method has been also used to analyse the VSA observations in the Corona Borealis supercluster region. Our method finds a clear deviation (99.82%) with respect to Gaussianity in the second-order moment of the distribution, and which can not be explained as systematic effects. A detailed study shows that the non-Gaussianity is produced in scales of $\ell \approx 500$, and that this deviation is intrinsic to the data (in the sense that can not be explained in terms of a Gaussian field with a different power spectrum). This result is consistent with the Gaussianity studies in the Corona Borealis data presented in Génova-Santos et al. (2005), which show a strong decrement

1 INTRODUCTION

The study of the Gaussianity of the primordial density fluctuations is a very important tool in constraining theories of structure formation. Inside the inflationary paradigm, there is a huge number of theories (see Bartolo et al. (2004) for a recent review on the subject), each one predicting different non-Gaussian signatures. Thus, any detection of non-Gaussianity would help to discriminate among these scenarios for the generation of cosmological perturbations. Because of this reason, the study of the Gaussianity of Cosmic Microwave Background (CMB) maps is becoming of major importance in modern cosmology. In particular, since the publication of the first year WMAP results (Bennett et al. 2003), several groups have tested the non-Gaussian nature of those maps using a wide set of techniques (Komatsu et al. 2003; Chiang et al. 2003; Eriksen et al. 2004a,b; Vielva et al. 2004; Park 2004; Cruz et al. 2005).

Furthermore, there are other reasons showing the importance of the study of the Gaussianity of the CMB. The majority of the inflationary models predict the primordial non-Gaussian signal to be smaller than the contribution from secondary effects such as gravitational lensing, reionization, Sunyaev-Zel'dovich effect, or the contribution of local foregrounds or unresolved point sources in the maps. Thus, tools to test Gaussianity could be used to trace the presence of these foregrounds. For example, the analysis of the WMAP data using the bispectrum allowed Komatsu et al. (2003) to perform estimates of the source number counts of unresolved sources in the 41 GHz channel (see also González-Nuevo et al. (2005)).

In addition, systematic effects may produce spurious detections of non-Gaussianities, so non-Gaussian methods could help in characterizing the properties of a given experiment (e.g. Banday et al. (2000)).

The Gaussianity of the VSA data was already examined using several methods in two separate papers (Savage et al. 2004; Smith et al. 2004), which were based on the data presented in Taylor et al. (2003) and Grainge et al. (2003). In Savage et al. (2004), a selection of non-Gaussianity tests are applied to the data. Most of these tests are based on real-space statistics and are applied to the maximum-entropy reconstruction of the regions observed by the instrument. In Smith et al. (2004), the analysis is devoted to the study of the bispectrum of the VSA data, showing how this statistic can be obtained in the case of interferometric experiments.

In this paper, we present the results of a Gaussianity analysis of the complete set of observations of the Very Small Array (VSA) dedicated to measure the CMB power spectrum (see Dickinson et al. (2004) and references therein), as well as an analysis of the data from the Corona-Borealis supercluster survey presented in Génova-Santos et al. (2005). Here, we will complement the previous Gaussianity studies of the VSA data by considering a different family of methods, called the Smooth Tests of Goodness of Fit (STGOF).

In section 2, we give a brief overview of the VSA experiment. In Section 3, we review the Smooth Tests of Goodness of Fit methods, and how these method can be adapted to the study of the Gaussianity of interferometric experiments. Section 4 describes how these methods can be further adapted to deal with large datasets or mosaiced observations. Section

‡ Present address: California Institute of Technology, Dept. of Astronomy, MS 105-24, 1200 E. California Blvd., Pasadena, CA 91125.

§ Present address: Astrophysics Group, Denys Wilkinson Building, University of Oxford.

¶ Present address: Astronomy Centre, University of Sussex, UK.

|| Present address: Faculty of Mathematics & Physics, University of Ljubljana, 1000 Ljubljana, Slovenia.

** Present address: Astrophysics Group, Denys Wilkinson Building, University of Oxford.

†† Present address: Instituto de Astrofísica de Canarias, 38200 La Laguna, Tenerife, Spain.

5 presents the calibration of the method using Gaussian simulations of mosaiced observations with the VSA. Section 6 presents the results of our analysis, and finally conclusions are presented in section 7.

2 THE VERY SMALL ARRAY

The VSA is a 14-element heterodyne interferometer sited at the Teide Observatory (Tenerife). The instrument is designed to image the CMB on scales going from 2° to $10'$, and operates at frequencies between 26 and 36 GHz with a 1.5 GHz bandwidth and a system temperature of ~ 30 K. The VSA has observed in two configurations of antennas. The first one is the so-called 'compact configuration', which covers the multipole range $\ell \sim 150 - 900$ with a primary beam of 4.6° -FWHM at 34.1 GHz. This configuration was used during the first observing season (September 2000- September 2001). The results of this campaign are presented in Watson et al. (2003); Taylor et al. (2003); Scott et al. (2003) and Rubiño-Martín et al. (2003).

The second one, the 'extended configuration', provided observations up to $\ell = 1500$ with a primary beam of 2.10° -FWHM (at 33 GHz) and an angular resolution of 11 arcmin during two separate campaigns. Those results were presented in two separate sets of papers: Grainge et al. (2003); Slosar et al. (2003) for the second season of observations (September 2001 - April 2002); and Dickinson et al. (2004); Rebolo et al. (2004) for the third one (April 2002- January 2003), where we obtained maps both at 34.1 GHz and at 33 GHz. With this extended configuration, we have obtained maps of a complete, X-ray flux-limited sample of seven clusters with redshifts $z < 0.1$ (Lancaster et al. 2005). We have also produced imaging at 33 GHz of the Corona-Borealis supercluster (Génova-Santos et al. 2005), with the aim of searching for Sunyaev-Zel'dovich detections from a possible extended signal due to diffuse warm/hot gas. As shown in that paper, we found a strong decrement near the centre of the supercluster, which can not be associated either with primordial CMB fluctuations or with a SZ effect from a known cluster of galaxies in the region. Therefore, we shall consider these data in our Gaussianity analysis as well.

In Table 1 we summarise the whole set of observations obtained with the VSA and used for cosmological studies, both with its compact and extended configurations. The full dataset comprises 8 fields observed with the compact array, and 33 fields observed with the extended one. This dataset can be arranged into seven separate (not overlapping) regions on sky, each of them obtained using mosaicing of individual pointings. Each mosaiced field is labeled as "VSA" plus a number. Within each mosaic, the names of the individual pointings are denoted by either no suffix, or the suffixes A, B, -OFF, E, F, G, H, J, K and L. Detailed information about the fields (central coordinates, integration times and maps) can be found in the indicated references. All these regions were carefully chosen to minimise contamination from Galactic emission and bright radio sources. Further details of the residual contamination in the maps can be found in Dickinson et al. (2004), and details about the VSA observational technique can be found in Watson et al. (2003).

Regarding the Corona Borealis observations, the core of

the supercluster is imaged with a 9 pointings mosaic, and we have two additional pointings outside this region to map two supercluster members which lie far from the optical centre of the supercluster. The total area covered is $\sim 24 \text{ deg}^2$ with an angular resolution of 11 arcmin and a sensitivity of 12 mJy/beam. Detailed information about the fields (central coordinates, integration times and maps) can be found in Génova-Santos et al. (2005).

2.1 Interferometer measurements

For observations of small patches of sky, we can adopt the flat-sky approximation and use Fourier analysis instead of the spherical harmonic expansion for the temperature field. In this limit, the *complex visibility* (which gives the response of an interferometer observing at frequency ν) can be written as

$$V(\mathbf{u}, \nu) = \int P(\hat{\mathbf{x}}, \nu) B(\hat{\mathbf{x}}, \nu) \exp(i2\pi \mathbf{u} \cdot \hat{\mathbf{x}}) d\hat{\mathbf{x}} \quad (1)$$

where $\hat{\mathbf{x}}$ is the angular position of the observed point on the sky; \mathbf{u} is the baseline vector in units of the wavelength of the observed radiation (so $2\pi \mathbf{u}$ is the Fourier mode); $P(\hat{\mathbf{x}}, \nu)$ is the primary beam of the antennas (normalised to unity at its peak); and $B(\hat{\mathbf{x}}, \nu)$ is the brightness distribution on the sky. For the case of CMB observations, this brightness can be expressed in terms of the equivalent thermodynamic temperature fluctuations ($\Delta T(\hat{\mathbf{x}})$) as

$$B(\hat{\mathbf{x}}, \nu) \approx \left. \frac{\partial B_\nu(T)}{\partial T} \right|_{T=T_0} \Delta T(\hat{\mathbf{x}}) \quad (2)$$

where $B_\nu(T)$ is the Planck function, and the mean temperature of the CMB is given by $T_0 = 2.726$ K (Mather et al. 1994).

By inserting the Fourier decomposition of the sky brightness in equation 1, we find that an interferometer measures the convolution of sky Fourier modes with the aperture function (Fourier transform of the primary beam), sampling at those points given by the projection of the baselines on the sky plane.

We note that the previous equation does not take into account the contribution of instrumental noise. Thus, for a realistic instrument observing at a frequency ν , the i th baseline \mathbf{u}_i of the interferometer will measure the following quantity

$$d(\mathbf{u}_i, \nu) = V(\mathbf{u}_i, \nu) + n(\mathbf{u}_i, \nu)$$

where $n(\mathbf{u}_i, \nu)$ stands for the instrumental noise on the \mathbf{u}_i visibility.

Let N be the total number of complex visibilities observed by an interferometer. Then, the complete set of observed visibilities will be noted as the following vector with $N_d = 2N$ elements

$$\mathbf{d} = \{\Re[d(\mathbf{u}_1, \nu_1)], \dots, \Re[d(\mathbf{u}_N, \nu_N)], \Im[d(\mathbf{u}_1, \nu_1)], \dots, \Im[d(\mathbf{u}_N, \nu_N)]\}$$

where the label \Re (\Im) stands for the real (imaginary) part of the complex number. We must note that in this equation, we explicitly differentiate the observing frequency for each observed sample because, in general, we could combine data

Table 1. Summary of the VSA observations dedicated to cosmological studies, and which have been analysed in this paper. We present the names for individual pointings contributing to one of the 7 VSA mosaics, separating the observations according to the three VSA campaigns. The central coordinates, integration times and maps for each of the individual pointings can be found in the three specified references.

Mosaic	Compact (Taylor et al. 2003)	Extended (Grainge et al. 2003)	Extended II (Dickinson et al. 2004)
VSA1	1, 1A, 1B	1E, 1F, 1G	1H, 1J, 1K, 1L
VSA2	2, 2-OFF	2E, 2F, 2G	2H, 2J, 2K, 2L
VSA3	3, 3A, 3B	3E, 3F, 3G	3H, 3J, 3K, 3L
VSA5	-	-	5E, 5F, 5G
VSA6	-	-	6E, 6F, 6G
VSA7	-	-	7E, 7F, 7G
VSA8	-	-	8E, 8F, 8G

taken at different frequencies with the same instrument (this is indeed the case of the VSA, in which we have observations at two different frequencies, 33 GHz and 34.1 GHz).

From here, we can also define the vector for the sky signal, and the vector for the noise in the same way, so we have $\mathbf{d} = \mathbf{V} + \mathbf{n}$. Assuming that there are no correlations between the sky signal and the noise, the covariance matrix for this set of observations can be written as

$$\mathbf{C} = \langle \mathbf{d} \mathbf{d}^t \rangle = \mathbf{S} + \mathbf{N}$$

where \mathbf{S} and \mathbf{N} are the covariance matrices of the contributions from the sky signal and the noise, respectively. In our analysis, we shall take this noise covariance matrix as diagonal, as is the case of the VSA data (e.g. Dickinson et al. (2004)).

The covariance matrix for the CMB component (\mathbf{S}) can be computed analytically using the equations presented in Hobson & Maisinger (2002), both for the case of a single or mosaiced observations. If the primary beam of the interferometer horns is symmetric respect to inversion through the origin (as it is the case of the VSA experiment, where the primary beam can be modelled to a good approximation by an spherical Gaussian function), then the aperture function is real. As a consequence, for the case of single-field observations the covariance matrix is block-diagonal (i.e. the real and imaginary parts of the visibilities are uncorrelated). Note that for mosaiced observations, this is not true in general.

3 GOODNESS-OF-FIT STATISTICS APPLIED TO INTERFEROMETERS

In this section we summarise some aspects of the smooth goodness-of-fit tests applied to CMB interferometers. For a more detailed description, see (Aliaga et al. 2005, hereafter, A05).

As shown in the previous section, the visibilities observed by an interferometer are correlated quantities. Therefore, the STGOF have to be adapted to deal with these data, because in their original form, these tests require independent data points. As described in A05, this is done following a two-step procedure. First, the data \mathbf{d} are transformed into signal-to-noise eigenmodes $\boldsymbol{\xi}$ (Bond 1995), and they are normalised. After this, the smooth goodness-of-fit tests developed by Rayner & Best (1989) can be applied to the nor-

malised eigenmodes, which for the Gaussian case would be independent.

3.1 Signal-to-noise eigenmodes

In a first step, the data are transformed into signal-to-noise eigenmodes as explained in A05. Every eigenmode has an associated signal-to-noise eigenvalue, in such a way that the higher is the value of the eigenvalue the more signal-to-noise ratio is associated to the eigenmode. Thus, this decomposition permits us not only to decorrelate the visibilities, but also to select those data points in which the signal contribution is dominating over that of the noise.

Let \mathbf{L}_n be the square root matrix of the noise correlation matrix (i.e. $\mathbf{N} = \mathbf{L}_n \mathbf{L}_n^t$), and \mathbf{R} the rotation matrix which diagonalizes the matrix

$$\mathbf{A} \equiv \mathbf{L}_n^{-1} \mathbf{S} \mathbf{L}_n^{-t} \quad (3)$$

Thus, $\mathbf{R}^t \mathbf{A} \mathbf{R} = \mathbf{E}$, where $\mathbf{E} = \text{diag}(E_1, \dots, E_{N_d})$ is a diagonal matrix whose diagonal elements are the signal-to-noise eigenvalues (E_i). With these definitions, the signal-to-noise eigenmodes are obtained as

$$\boldsymbol{\xi} = \mathbf{R}^t \mathbf{L}_n^{-1} \mathbf{d} \quad (4)$$

From here, it is easy to show that the covariance matrix associated to these variables is given by $\langle \boldsymbol{\xi} \boldsymbol{\xi}^t \rangle = \mathbf{E} + \mathbf{I}_{N_d}$, where \mathbf{I}_{N_d} is the identity matrix with dimension $N_d \times N_d$.

The normalised signal-to-noise eigenmodes can be defined from here as $y_i = \xi_i / (E_i + 1)^{1/2}$ ($i = 1, \dots, N_d$), and one can immediately show that these quantities are uncorrelated and they verify $\langle y_i y_j \rangle = \delta_{ij}$.

For our case of interest (CMB analyses), the important point is that equation 4 is a linear transformation, so it preserves the Gaussianity of the variables (i.e. if the data \mathbf{d} are distributed following a multi-normal function, then the normalised eigenmodes will follow a one-dimensional Gaussian distribution $N(0, 1)$). Thus, one can now apply the STGOF to these transformed variables.

3.2 Smooth tests of goodness-of-fit

Let us assume that we have n independent realizations $\{x_i\}_{i=1}^n$ of a statistical variable x , and we want to test if x has a distribution function compatible with $f(x)$ (null hypothesis). Rayner & Best (1989) proposed some statistics to

discriminate between f and another distribution (alternative hypothesis) which deviates smoothly from f . In the case in which f is a Gaussian ($N(0, 1)$), it can be shown that the first four score statistics associated with the alternative are given by

$$S_k = \sum_{i=1}^k U_i^2 \quad (5)$$

with

$$\begin{aligned} U_1^2 &= n(\hat{\mu}_1)^2 \\ U_2^2 &= n(\hat{\mu}_2 - 1)^2/2 \\ U_3^2 &= n(\hat{\mu}_3 - 3\hat{\mu}_1)^2/6 \\ U_4^2 &= n[(\hat{\mu}_4 - 3) - 6(\hat{\mu}_2 - 1)]^2/24 \end{aligned} \quad (6)$$

where $\hat{\mu}_\alpha = (\sum_{j=1}^n x_j^\alpha)/n$ is the estimated moment of order α . It should be noted that this test is *directional*, i.e. it indicates how the actual distribution deviates from Gaussianity.

If the data are drawn from the distribution given by f , and n is large enough ($n \gtrsim 100$), then it is possible to show that the U_i^2 quantities are distributed following a χ^2 with one degree of freedom. If the data do not follow an f distribution, we expect departures from this distribution, and this is the way we detect non-Gaussian signals.

We shall apply these statistics to the normalised eigenmodes described in the last subsection. The important point for us is that, as shown in A05, we can select subsets of signal-to-noise eigenmodes, according to their associated eigenvalue E_i . This will permit us to test if $y_i \sim N(0, 1)$ (that is, our null hypothesis is that f is a Gaussian function).

4 EXTENDING THE METHOD TO MOSAICED FIELDS. THE ARNOLDI ALGORITHM

The method we have applied in the previous sections only uses a few eigenmodes (the ones whose eigenvalue is large enough), but the correlation matrices are relatively large (matrices from 5000×5000 to 10000×10000 for the mosaic analysis). This implies a big computational cost in the diagonalization of the matrices. Thus, we pose the following question: is it possible to reduce the dimension of the correlation matrix to calculate only those eigenmodes and eigenvalues we need?

There are several numerical methods for solving eigenvalue problems with large matrices. We shall consider here one particular class of methods, named the Krylov subspace methods, and in particular the Arnoldi algorithm. This method can be applied to general non-Hermitian matrices, although we will focus here in the application to our problem, in which the covariance matrix is real and symmetric, and has a sparse structure. Our development is based on Saad (1992) (see also Aliaga (2005)).

4.1 The Arnoldi method

This procedure was introduced as a means of reducing a dense matrix into Hessenberg form (lower triangular matrix). However, the important point for us is that this

method was shown to be a good technique for approximating the eigenvalues of large sparse matrices.

The basis of the method is as follows. We start from our sparse matrix \mathbf{A} given in equation 3, which has dimensions $N_d \times N_d$. Then, we want to build a new matrix \mathbf{H} with dimensions $m \times m$, in such a way that $m < N_d$ and the eigenvalues/eigenvectors of \mathbf{H} should be approximations to the eigenvalues/eigenvectors of \mathbf{A} (it is obvious that we will not recover all the eigenvalues, but only m at the most).

The algorithm produces a set of vectors, $\{\mathbf{q}_1, \dots, \mathbf{q}_m\}$, which form an orthonormal basis of the subspace linear span of $\{\mathbf{q}_1, \mathbf{A}\mathbf{q}_1, \dots, \mathbf{A}^{m-1}\mathbf{q}_1\}$. One variant of this algorithm for real and symmetric matrices will be presented below. From these vectors, we can build the following $(N_d \times m)$ -matrix

$$\mathbf{Q}_{ij} \equiv (\mathbf{q}_j)_i, \quad i = 1, \dots, N_d; \quad j = 1, \dots, m$$

with $(\mathbf{q}_j)_i$ the i th component of the j th vector. The matrix in which we are interested can be derived as

$$\mathbf{H} = \mathbf{Q}^\dagger \mathbf{A} \mathbf{Q} \quad (7)$$

where \dagger stands for the transpose conjugate matrix¹. The \mathbf{H} matrix has an upper triangular form, and can be diagonalized to find its eigenvalues $E_i^{(H)}$ and associated eigenvectors $\mathbf{y}_i^{(H)}$. From here, we can build the *Ritz approximate eigenvectors* associated to $E_i^{(H)}$ as $\mathbf{e}_i^{(H)} = \mathbf{Q}\mathbf{y}_i^{(H)}$. The important point for us is that a fraction of these Ritz eigenvectors are a good approximation of the corresponding eigenvectors of \mathbf{A} , and at the same time, $E_i^{(H)}$ give a good approximation to the associated eigenvalue E_i . Moreover, the quality of the approximation improves as m increases.

We note that there are simple analytical expressions for the residual norm associated to the Ritz eigenvectors. These expressions can be easily implemented in the algorithm, so one controls the quality of the approximations (Saad 1992; Aliaga 2005).

4.2 Signal-to-noise eigenmodes

We show now how to use signal-to-noise eigenmodes together with the Arnoldi method.

Let $\mathbf{R}^{(H)}$ be the rotation matrix which diagonalizes \mathbf{H} . $\mathbf{R}^{(H)}$ is constructed in such a way that its i th column corresponds to the $\mathbf{y}_i^{(H)}$ eigenmode defined in the previous subsection (i.e. $\mathbf{R}_{ij}^{(H)} = (\mathbf{y}_j^{(H)})_i$). Then,

$$(\mathbf{R}^{(H)})^t \mathbf{H} \mathbf{R}^{(H)} = \text{diag}(E_1^{(H)}, \dots, E_m^{(H)}) \equiv \mathbf{E}^{(H)} \quad (8)$$

We now define the matrix $\mathbf{T} = \mathbf{Q}\mathbf{R}^{(H)}$, which has dimensions $N_d \times m$. Hence, using equations 7 and 8 we have

$$\mathbf{T}^t \mathbf{A} \mathbf{T} = \mathbf{E}^{(H)}$$

Using these matrices, the signal-to-noise eigenmodes can be defined as

$$\boldsymbol{\xi}^{(H)} = \mathbf{T}^t \mathbf{L}_n^{-1} \mathbf{d} \quad (9)$$

and the corresponding correlation matrix can be written as $\langle \boldsymbol{\xi}^{(H)} (\boldsymbol{\xi}^{(H)})^t \rangle = \mathbf{E}^{(H)} + \mathbf{I}_m$. The transformed signal and noise vectors are given here by $\tilde{\mathbf{V}} = \mathbf{T}^t \mathbf{L}_n^{-1} \mathbf{V}$ and

¹ In our case, \mathbf{A} is real, so we could use transpose instead of transpose conjugate.

$\tilde{\mathbf{n}} = \mathbf{T}^t \mathbf{L}_n^{-1} \mathbf{n}$, such that $\langle \tilde{\mathbf{V}} \tilde{\mathbf{V}}^t \rangle = \mathbf{E}^{(H)}$ and $\langle \tilde{\mathbf{n}} \tilde{\mathbf{n}}^t \rangle = \mathbf{I}_m$. Therefore, the meaning of the signal-to-noise eigenmodes is preserved, and eigenmodes associated to large eigenvalues have more contribution from the signal than from the noise.

As indicated in the previous subsection, some of the eigenvalues $E_i^{(H)}$ will also be eigenvalues of \mathbf{A} to a good approximation. Moreover, as we shall see below, those eigenvalues which are better approximated will correspond to high values of the signal-to-noise eigenvalue. Thus, this method will permit to estimate the eigenvalues (and the associated signal-to-noise eigenmodes) which are of interest for our analysis, but the dimensionality of the problem will be greatly reduced. Finally, let us note that with the previous definition of signal-to-noise eigenmodes associated to \mathbf{H} , they will directly give a good approximation to the corresponding eigenmodes for \mathbf{A} .

4.3 Relationship between the matrices which diagonalize \mathbf{H} and \mathbf{A}

From the definition of the signal-to-noise eigenvectors given in equation 9, it is clear that if a pair $E_i^{(H)}, \mathbf{e}_i^{(H)}$ (an eigenvalue and its associated Ritz eigenvector) is a good approximation to the corresponding pair for the \mathbf{A} matrix, then $\xi_i^{(H)}$ will give a good approximation to ξ_i as well. However, there is a sign ambiguity when implementing this algorithm in practice. When obtaining the eigenvectors for a given matrix, we impose that it should be unitary, but an ambiguity in the sign is still present (if \mathbf{y} is an eigenvector, then $-\mathbf{y}$ is an eigenvector as well).

This ambiguity can be avoided by imposing an additional condition, for example, that the first component different from zero of each eigenvector should be positive (in fact, due to precision problems, it is better to impose that the component which is the maximum in absolute value for each eigenvector should be positive). With this criterion, then it is clear that the statistics of the smooth goodness-of-fit tests of Rayner & Best (1989) can be computed from the signal-to-noise eigenmodes of \mathbf{H} , yielding exactly the same values as those computed from \mathbf{A} if they only involve those eigenvectors whose associated eigenvalues are correctly approximated. In the next two subsections we present an example of implementation of this method, and we apply it to the case of simulated VSA observations.

4.4 Lanczos algorithm

This is a particular simplification of the Arnoldi algorithm for the case when the considered matrix is Hermitian. In this case, it can be shown that the \mathbf{H} matrix is real, tridiagonal and symmetric. Thus, the algorithm becomes computationally faster, and fewer variables need to be stored in memory. The implementation of the algorithm that we have used here is the following:

(i) **Start.** We choose an initial unitary vector \mathbf{q}_1 , and we define $H_{01} = 0, \mathbf{q}_0 = 0$.

(ii) **Iterate.** For $j = 1, \dots, m$:

$$\mathbf{w} = \mathbf{A} \mathbf{q}_j - H_{j-1,j} \mathbf{q}_{j-1} \quad (10)$$

$$H_{jj} = \mathbf{q}_j^\dagger \mathbf{w} \quad (11)$$

$$\mathbf{w} = \mathbf{w} - H_{jj} \mathbf{q}_j \quad (12)$$

$$H_{j,j+1} = \|\mathbf{w}\| \quad (13)$$

$$\mathbf{q}_{j+1} = \mathbf{w} / H_{j,j+1} \quad (14)$$

In the previous algorithm, the symbol $\|\cdot\|$ represents the Euclidean norm of a vector, and it is defined as $\|\mathbf{x}\| \equiv (\mathbf{x}^\dagger \mathbf{x})^{1/2}$, where the symbol \dagger stands for the transpose conjugate operator.

The above algorithm guarantees that the \mathbf{q}_i vectors are orthogonal. However, when m is relatively large, the orthonormality of the \mathbf{q}_i vectors is lost, so they have to be orthonormalised as they are calculated (for example using the method of Gram-Schmidt). We note that if \mathbf{A} is sparse (as is our case), then there are algorithms to optimise the product operation $\mathbf{A} \mathbf{q}_j$, and therefore the iterative process can be accelerated (see Saad (1992)).

5 CALIBRATION OF THE METHOD WITH SIMULATED VSA MOSAICED OBSERVATIONS

The STGOF have been already applied to simulated observations of the VSA in A05, showing the ability of the method to detect non-Gaussian signals introduced via the Edgeworth expansion, cosmic strings or χ^2 -simulations, when we use realistic noise levels from the experiment. In that paper, the analysis was performed by simulating a single VSA pointing, and setting the noise levels according to the typical integration time of the fields. In order to complete this picture, we present here the calibration of the method by using simulated Gaussian mosaiced observations. There is no difference in practice between analysing single and mosaiced fields, so the results will be similar to those found in A05. However, this study will permit us to test the software for computing covariance matrices in mosaiced observations. This software evaluates the covariance matrix from a given power spectrum, using the equations presented in Hobson & Maisinger (2002).

A visibility file of an individual pointing typically contains $10^5 - 10^6$ visibility points. Thus, we need to bin the data into cells of certain size prior to the Gaussianity analysis. For this paper, we have adopted the same bin size and binning procedure used for the determination of the power spectrum (see Scott et al. (2003) and Grainge et al. (2003)). Thus, the compact array data were binned using a cell size of 4λ , where λ is the observing wavelength, whereas for the extended array we used 9λ . Tests with different cell sizes were done in A05, showing that there are no significant changes in the results when varying these values.

5.1 Gaussian simulations

To illustrate the method in the case of mosaiced observations, we used the VSA1 mosaic with the extended configuration (Grainge et al. 2003). This mosaic contains three individual pointings (VSA1E, VSA1F and VSA1G). After binning using 9λ cells, the data files contain 914, 882 and 911 complex visibility points, respectively. Thus, the covariance matrix has in this case a size of $N_d = 5414$ ($N = 2707$).

We performed 10000 Gaussian simulations of this three-pointings mosaic, including Gaussian CMB signal plus

Table 2. Values of the mean ($\langle U_i^2 \rangle$) and the standard deviation (σ) of the statistics U_i^2 for 10000 Gaussian CMB plus noise simulations of the VSA1 extended mosaic. They are compared with the corresponding asymptotic values (for χ_1^2), displayed in last column. We show the results for two different values of E_{cut} . The numbers within parenthesis indicate the number of eigenvalues with $E_i \geq E_{cut}$.

	U_1^2	U_2^2	U_3^2	U_4^2	χ_1^2
$E_{cut} = 0$ (5414 data)					
$\langle U_i^2 \rangle$	1.01	0.99	1.00	0.99	1.00
σ	1.42	1.39	1.40	1.41	$\sqrt{2}$
$E_{cut} = 0.4$ (219 data)					
$\langle U_i^2 \rangle$	1.00	1.02	0.98	0.99	1.00
σ	1.38	1.42	1.47	2.03	$\sqrt{2}$

Gaussian noise, according to the noise levels of the real observations. The power spectrum adopted for the simulations, as well as for their analysis, corresponds to the one presented in Dickinson et al. (2004).

Fig. 1 shows the histogram of the obtained U_i^2 values, and compares it with the expected χ_1^2 distribution. As expected, the U_i^2 quantities are distributed following a χ_1^2 . Table 2 presents the mean value and the standard deviation of these U_i^2 quantities. As we will see below, we will focus our analysis on those values for the statistics which are computed using a subset of the signal-to-noise eigenmodes with high signal-to-noise ratios, i.e. using only those eigenmodes with associated eigenvalues satisfying $E_i \geq E_{cut}$. In particular, we will use the value of $E_{cut} = 0.4$, so we present here the results both for $E_{cut} = 0$ and $E_{cut} = 0.4$. In this second case, we keep only $\sim 4\%$ of the data (219 points), so this is why the distribution of U_4^2 is slightly broader than the asymptotic value of $\sqrt{2}$.

In order to illustrate the sensitivity of the method to the power spectrum used in the computation of the covariance matrix, we have done the following test. Using the measured power spectrum from Dickinson et al. (2004), we have created three mock power spectra, two of them defined by the envelope of the 1-sigma error bars of the data, and the third one as an intermediate case connecting alternate values of +1 and -1 sigma, as shown in Figure 2. We call the “upper power spectrum” (“lower power spectrum”) the one derived linking the measured data points plus (minus) one sigma, while the “oscillating power spectrum” is the one derived linking the alternate measured data points plus/minus one sigma.

We use these power spectra to analyse the previous 10000 simulations (which were generated using the measured power spectrum). The mean values and the standard deviations of the U_i^2 quantities are shown in Tables 3, 4 and 5, respectively. These test cases show us how the distribution of the U_i^2 quantities is changing due to the use of an incorrect power spectrum. Overall deviations of the power with respect to the true power spectrum always appear as an excess in the U_2^2 statistic. Therefore, such an excess in U_2^2 can reflect either an intrinsic non-Gaussianity or a deviation of the local power spectrum from the averaged one

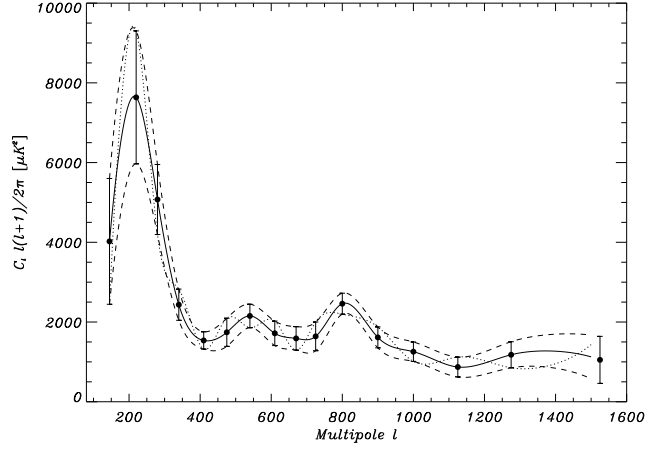


Figure 2. Power spectrum used in the simulations. The data points correspond to the data presented in Dickinson et al. (2004), but no correction due to residual sources and Galactic foregrounds have been applied. The solid line is a spline interpolation of the data points, whereas the dashed lines are obtained interpolating the regions of +1 sigma and -1 sigma. The dotted line corresponds to an intermediate case, where we connect alternate values of plus and minus one sigma.

Table 3. Same as Table 2, but now the 10000 simulations are analysed using the lower fit power spectrum explained in the text.

	U_1^2	U_2^2	U_3^2	U_4^2	χ_1^2
$E_{cut} = 0$ (5414 data)					
$\langle U_i^2 \rangle$	0.98	1.18	1.00	1.04	1.00
σ	1.37	1.67	1.41	1.59	$\sqrt{2}$
$E_{cut} = 0.4$ (198 data)					
$\langle U_i^2 \rangle$	1.13	2.44	1.37	1.56	1.00
σ	1.57	3.24	2.18	3.77	$\sqrt{2}$

(i.e. anisotropy). However, the third test case shows that if our power spectrum deviates from the real one in a “realistic way”, then we do not expect a significant effect on the mean value of U_2^2 statistic². This is an important point, because a too strong dependence on the input power spectrum would make this method difficult to apply in practice.

² However, we note that for this particular case in which the “wrong” power spectrum oscillates around the real one, we find an effect in the mean value of U_4^2 for $E_{cut} = 0.4$, where we have $\langle U_4^2 \rangle = 0.90$ with an error $1.69/\sqrt{10000} \approx 0.02$. This shows that although the average band power is approximately the same as the true value (and thus we do not detect a significant effect on U_2^2), the different shape of the power spectra inside each bin is detected in the higher moments (U_4^2).

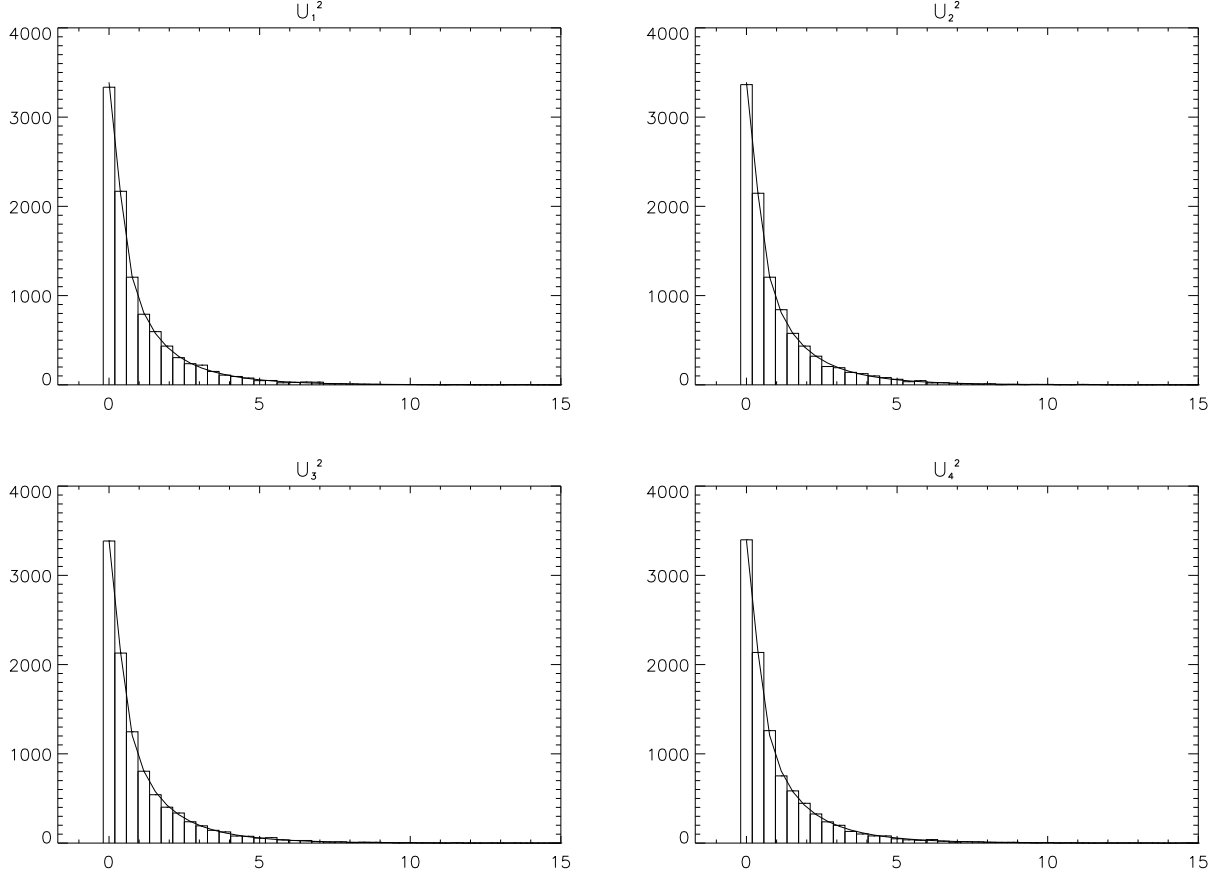


Figure 1. Distributions of the U_i^2 statistics, from left to right, top to bottom $i = 1, 2, 3, 4$, when using only $E_i > 0.4$. They are obtained from 10000 simulated observations of the VSA1 mosaic, so each simulation contains three individual pointings which partially overlap on sky. The simulations contain Gaussian CMB signal plus the realistic noise achieved in the observations. Prior to the analysis, the visibilities are binned in cells of 9λ in Fourier space. The solid line shows the expected values from a χ_1^2 distribution normalised to the total number of simulations.

Table 4. Same as Table 2, but now the 10000 simulations are analysed using the upper fit power spectrum explained in the text.

	U_1^2	U_2^2	U_3^2	U_4^2	χ_1^2
$E_{cut} = 0$ (5414 data)					
$\langle U_i^2 \rangle$	0.99	1.08	0.98	0.96	1.00
σ	1.37	1.67	1.41	1.59	$\sqrt{2}$
$E_{cut} = 0.4$ (243 data)					
$\langle U_i^2 \rangle$	0.89	1.79	0.75	0.71	1.00
σ	1.44	1.49	1.39	1.47	$\sqrt{2}$

Table 5. Same as Table 2, but now the 10000 simulations are analysed using the oscillating power spectrum explained in the text.

	U_1^2	U_2^2	U_3^2	U_4^2	χ_1^2
$E_{cut} = 0$ (5414 data)					
$\langle U_i^2 \rangle$	0.99	0.99	1.02	1.00	1.00
σ	1.44	1.39	1.41	1.44	$\sqrt{2}$
$E_{cut} = 0.4$ (220 data)					
$\langle U_i^2 \rangle$	0.97	1.01	0.96	0.90	1.00
σ	1.35	1.40	1.46	1.69	$\sqrt{2}$

5.2 Example of application of the Arnoldi method to VSA data

We show now an example of application of the Arnoldi method to the VSA data, and we present the result of the analysis of the VSA2 mosaic observed in the first campaign of the extended configuration. We have performed this

analysis using both the standard method and the Arnoldi method.

This mosaic is built up from three individual pointings, with names VSA2E, VSA2F and VSA2G. The total number of visibility points for this mosaic, once the data are binned into 9λ cells, is 2751, so the dimension of the matrix \mathbf{A} in

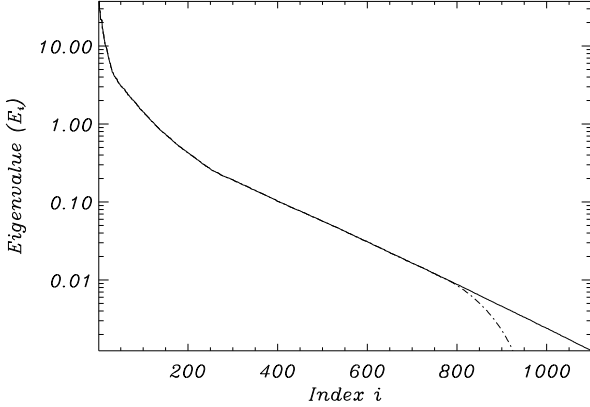


Figure 3. Example of application of the Arnoldi method. We show the eigenvalues corresponding to the analysis of a mosaiced field with 5502 data points. We have applied the Lanczos implementation using $m = 1000$. The solid line shows the eigenvalues (E_i) of \mathbf{A} derived from the analysis of the full covariance matrix, while the dot-dashed line shows the eigenvalues (E_i) of \mathbf{H} from the Arnoldi method.

this case is $p = 5502$. We have considered here the case of $m = 1000$.

Figure 3 shows the comparison of the eigenvalues derived using both methods. The eigenvalues of \mathbf{A} are represented by the solid line, while the eigenvalues of \mathbf{H} are displayed by the dot-dashed line. We can see that the highest eigenvalues are recovered very well, but when we approach to the dimension of the \mathbf{H} matrix ($m=1000$), then the recovered eigenvalues departure from real values. In this particular case, all eigenvalues with index $i < 773$ are recovered with a relative error smaller than 0.1%, while for $i < 787$ the error is smaller than 1%. In general, when the exact values of the eigenmodes are unknown, the errors are controlled with the residual norm associated to the Ritz eigenvectors (Saad 1992).

We note that for $E_{cut} = 0.4$, the first 228 eigenvalues are inside this cut. As we will see below, we will use this value for the analysis. Therefore, for our purposes an analysis using the Arnoldi method will provide exactly the same results for the U_i^2 quantities as the full analysis.

6 GAUSSIANTY ANALYSIS OF VSA DATA

In this section, we present the results of the non-Gaussianity analysis of the VSA data using the STGOF. The method has been applied to the list of pointings quoted in Section 2, considering both the individual pointings separately, or arranging them into the corresponding mosaics. For each analysis, the U_i^2 statistics were obtained for different values of E_{cut} , ranging from 0 to 0.5.

In all cases (except for the Corona-Borealis mosaic), the analysis was performed using both the standard procedure (full diagonalization of the covariance matrix) and the Lanczos algorithm with $m = 1000$. We have checked that the values of the statistics (U_i^2) derived from both methods are exactly the same for those cuts with $E_{cut} \geq 0.1$, and

there are small differences for $0.1 \gtrsim E_{cut} \gtrsim 0.01$. However, the standard computation was more time consuming than the Lanczos algorithm. For example, once the covariance matrix is computed, the typical computing time for the diagonalization of a matrix with $N_d = 7200$ was ≈ 1.2 hours in a 2.6 GHz Processor with 2 GHz RAM, and this number scales roughly as N_d^3 . However, the Lanczos algorithm with $m = 1000$ takes only 15 s in the diagonalization step.

The power spectrum used to compute the covariance matrices corresponds to the one derived from the data (Dickinson et al. 2004), and presented as a solid line in Fig. 2. As mentioned above, the data files are binned in the visibility space into cells of 4λ for the compact array data, and 9λ for the extended array data.

Given the huge number of statistics we obtained, we proceed as follows in order to present a comprehensive summary of the analysis. We shall present our results only for the analyses of the mosaiced observations, and we shall quote the values and the significance of the U_i^2 statistics for the eigenvalue cut $E_{cut} = 0.4$. High values of E_{cut} are desirable because we select eigenmodes with higher signal-to-noise ratios, and for these values the statistical properties of the signal are not diluted by the noise. However, if the value of E_{cut} is too high, then we end up with a small number of data-points. As shown in A05, for the signal-to-noise ratio achieved in a VSA field, this cut for the eigenvalues uses a reasonable number of data points ($\sim 10\%$), and at the same time it gives good results in discriminating non-Gaussian signal obtained from the Edgeworth expansion and from string simulations. In any case, we have checked that there are no significant differences if we change the value of E_{cut} in the range 0.1 to 0.5.

If a non-Gaussian signal is detected in a given mosaic, we follow these steps

- a) We present the values of the statistics for the individual fields, in order to identify and localise the pointing(s) responsible of the non-Gaussian signal.
- b) Data corresponding to those individual pointings containing the non-Gaussian signal are split into two parts, corresponding to different epochs of observation. The analysis is performed in each one of these two parts, in order to isolate possible residual systematic effects.
- c) Those individual pointings are also analysed by splitting the data into separate regions of the uv-plane, so one can localise the origin of the signal in Fourier space. To allow a simple identification of the Fourier regions, we divided the uv-plane into 16 concentric annuli. The edges of these annuli are taken from the bins adopted in Dickinson et al. (2004) to present the power spectrum results, and are quoted in Table 6 (note that $\ell = 2\pi|\mathbf{u}|$).
- d) The VSA collaboration has always maintained two independent pipelines, so every pointing has been reduced in parallel by at least two of the three institutions. Thus, if a non-Gaussian signal is detected in a given mosaic, we also checked the second (independent) version of the reduction of the data, to identify if the non-Gaussian signal was due to residual systematic effects.
- e) Finally, we have also explored the robustness of the results when using different noise estimates for the visibilities. Within the VSA collaboration, we have used two different noise estimates, one based on daily estimates from the scat-

Table 6. Multipole bins considered in our analysis. The quoted values correspond to the same bin limits used in the power spectrum estimation, as presented in Dickinson et al. (2004).

Bin	ℓ_{\min}	ℓ_{\max}
1	100	190
2	190	250
3	250	310
4	310	370
5	370	450
6	450	500
7	500	580
8	580	640
9	640	700
10	700	750
11	750	850
12	850	950
13	950	1050
14	1050	1200
15	1200	1350
16	1350	1700

ter on the visibility data in each baseline, and another one based on the scatter of the visibilities when they are binned into cells prior to the power spectrum computations (see the details in Taylor et al. (2003)). These two methods have been shown to produce consistent results on the power spectra, but we shall explore here whether those non-Gaussian signals could be understood using a different noise characterization.

Data has been split according to the configuration of the instrument (compact or extended data). This will permit us to isolate possible systematic effects which could be only present in a given configuration. For the extended array dataset, we also split the data into two subgroups, which correspond to the dataset presented in Grange et al. (2003), and the rest of the VSA extended fields described in Dickinson et al. (2004). This allows a direct comparison of our results for the extended array with those from the previous papers (Savage et al. 2004; Smith et al. 2004) on the same datasets.

Our results are presented in Table 7, for the case of $E_{\text{cut}} = 0.4$. The total number of visibility points in the binned files is also shown in the second column of that table. All the results are compatible with a Gaussian distribution, except in three cases where we obtain values for the statistics with a significance greater than 95%. These cases are the mosaics for the VSA2 and VSA3 fields obtained with the first release of the extended configuration (fields VSA2E, VSA2F and VSA2G, and VSA3E, VSA3F and VSA3G, respectively), and the Corona-Borealis mosaic (quoted as CoronaB). In these three cases, there is apparently a detection with the U_2^2 statistic, which may indicate either a deviation from the theoretical power spectrum or a non-Gaussian signature (as shown for instance for cosmic strings in A05). We now discuss each of these three cases in detail.

6.1 VSA2 mosaic, extended configuration

An individual analysis of the three fields of the mosaic shows that VSA2E is compatible with gaussianity ($U_2^2 = 2.46(88.3\%)$), while the VSA2F ($U_2^2 = 10.3(99.9\%)$) and VSA2G ($U_2^2 = 17.0(100\%)$) present a strong deviation.

If we now split the VSA2F and VSA2G datasets into two parts, corresponding to two separate epochs, we find that the non-Gaussian signal is present in both of them, and for both pointings. This result suggests that the origin of the signal is intrinsic to the data, because it can not be isolated in a separated epoch. In order to localise the origin of this signal in Fourier space, we performed the analysis using the 16 anulli regions mentioned above, and defined in Table 6. In order to keep a reasonable number of data points in this “bin analysis”, we now use a lower value for $E_{\text{cut}} (= 0.1)$. The detailed analysis shows that the non-Gaussian signal in U_2^2 associated with VSA2F is localised in bins 9 and 11, while the non-Gaussianity associated to VSA2G comes from bins 9, 10 and 11.

The following step, in order to cross-check these results, is to use the independent reduction of these two pointings that we produced in the collaboration. An analysis of this second version of the data shows that both VSA2F and VSA2G present a deviation on U_2^2 , although in the case of the VSA2F pointing this deviation is smaller ($U_2^2 = 5.1(97.6\%)$). We have also checked that these non-Gaussianity detections are robust against the two different schemes for noise estimation. Moreover, varying the noise estimates for the data within a $\pm 5\%$ does not change the results on the U_2^2 statistic.

6.1.1 Study of the local power spectrum

The previous tests suggest that the non-Gaussian signal detected in the data via the U_2^2 statistic could be real, and not due to systematics. Given that U_2^2 may indicate deviations on the second moment of the (transformed) visibilities, we have investigated the power spectrum of these two fields, as well as that of the VSA2EFG mosaic.

We have used for this computation 8 bins instead of 16 because the thermal noise in a single VSA field is high, so using small amount of visibilities could bias the estimation of the power. The 8 bins were obtained by joining the sixteen bins from Table 6 in pairs, so one can easily relate the new bins with the old ones (i.e. the new bin 1 corresponds to bins 1 and 2 from that table, and so on).

The power spectrum of the VSA2EFG field is found to be compatible (at the 1-sigma level) with the one presented in Dickinson et al. (2004), except in two bins which correspond with bins 9 & 10, and 11 & 12 from Table 6, and where we find a 2.1-sigma and 1.5-sigma deviation toward higher values, respectively (see Fig. 4). Although noisy, the power spectrum of the individual fields (VSA2F and VSA2G) also show a deviation on those scales, being larger in the VSA2G case (practically 2-sigma). The VSA2E field shows no deviations. A visual inspection of the VSA2 extended I mosaic (see figure 3 in Dickinson et al. 2004) shows an intense positive feature close to the centre of the G pointing, which could be the responsible for that deviation.

In order to check if these fields are intrinsically Gaussian, we have analysed the VSA2EFG mosaic using now

Table 7. Values for the U_i^2 statistics and their corresponding probabilities (within parenthesis) derived from the χ^2 distribution from the analysis of the VSA mosaiced fields, using the cut $E_{cut} = 0.4$. Second column shows the number of visibility points (N) after binning the VSA data, prior to the Gaussianity analysis. The size of the covariance matrix is $N_d \times N_d$, with $N_d = 2N$. The three cases where we have a non-Gaussian detection are marked using bold characters.

Mosaic	N	U_1^2	U_2^2	U_3^2	U_4^2
VSA1 (compact)	4071	0.51 (52.6%)	0.61 (56.5%)	0.08 (21.9%)	1.45 (77.1%)
VSA2 (compact)	3645	0.63 (57.4%)	2.43 (88.1%)	0.16 (30.7%)	0.00 (3.03%)
VSA3 (compact)	4715	1.37 (75.9%)	0.19 (33.5%)	0.86 (64.7%)	1.27 (74.1%)
VSA1 (extended I)	2707	0.01 (7.06%)	2.40 (87.9%)	0.26 (39.2%)	0.07 (20.9%)
VSA2 (extended I)	2751	1.93 (83.5%)	8.50 (99.7%)	0.22 (36.3%)	2.88 (91.0%)
VSA3 (extended I)	2925	0.56 (54.5%)	7.49 (99.4%)	0.26 (38.8%)	0.39 (46.6%)
VSA1 (extended II)	4174	0.01 (7.62%)	0.37 (45.7%)	0.25 (38.0%)	0.03 (13.8%)
VSA2 (extended II)	4384	0.06 (19.0%)	1.34 (75.2%)	0.19 (33.5%)	1.53 (78.3%)
VSA3 (extended II)	4297	0.00 (0.46%)	2.23 (86.4%)	0.13 (27.8%)	0.00 (4.53%)
VSA5 (extended II)	2485	0.03 (13.3%)	2.26 (86.8%)	0.07 (21.1%)	0.16 (31.2%)
VSA6 (extended II)	2531	2.98 (91.6%)	1.13 (71.2%)	0.51 (52.5%)	0.37 (45.7%)
VSA7 (extended II)	2611	0.08 (22.9%)	0.16 (31.2%)	0.06 (20.0%)	0.00 (4.50%)
VSA8 (extended II)	2919	0.12 (27.4%)	0.58 (55.3%)	0.00 (2.17%)	0.06 (19.1%)
CoronaB (extended II)	6629	0.01 (6.21%)	9.79 (99.82%)	0.26 (38.70%)	0.08 (21.75%)

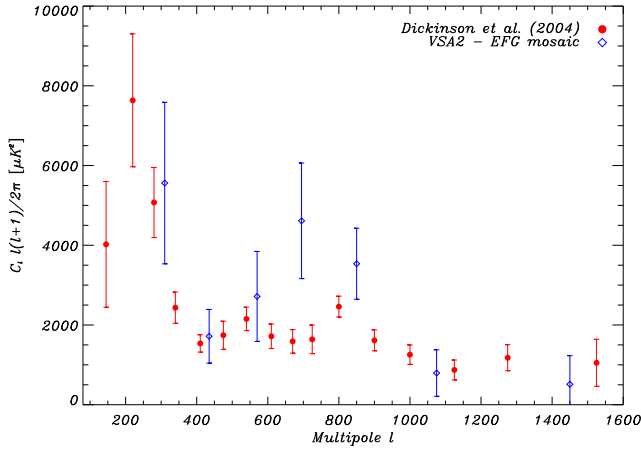


Figure 4. Power spectrum of the VSA2 mosaic observed with the extended I configuration (pointings VSA2E, VSA2F and VSA2G). Although noisy (there are only three pointings entering in the computation), we can see a deviation with respect to the Dickinson et al. result, at angular scales corresponding to $\ell \approx 700 - 900$.

its own power spectrum. In this case, we find the value $U_2^2 = 1.01(68.38\%)$ for $E_{cut} = 0.4$, which is now compatible with Gaussianity. These results suggest that the U_2^2 excess found in this case is connected with a deviation of the power spectrum of the region with respect to the average one, and not with an intrinsic non-Gaussianity (in the sense that when we perform the analysis using their power spectrum, then they are Gaussian).

To complete our study with the STGOF, we have investigated how significant is that deviation of the power spectrum of the region with respect to the average power spectrum. The probability of finding such a deviation in a multivariate Gaussian field can be easily derived by noting

that the 8 bins used in the power spectrum computation are practically independent. Using Monte Carlo simulations, we estimate that with the measured band powers and errors, the probability of having 2 numbers out of 8 such that one of them deviates 2.1-sigma and the other one 1.5-sigma is 4.6%. If we now impose that these two values should be in adjacent bins (as is our case), then this value reduces to 1.4%. Given that we have observed 13 mosaics with similar characteristics (although not completely independent, because mosaics 1, 2 and 3 for different configurations partially overlap), then we conclude that this deviation of the power spectrum is not as significant as the one obtained using the U_2^2 statistic. In any case, both analyses suggest that we have detected a local deviation of the power spectrum (i.e. an anisotropy) in this VSA2 mosaic.

6.2 VSA3 mosaic, extended configuration

An individual analysis of the three fields contained in the mosaic shows that VSA3F is compatible with gaussianity ($U_2^2 = 0.52(52.8\%)$), while the VSA3E ($U_2^2 = 5.48(98.1\%)$) and VSA3G ($U_2^2 = 5.89(98.5\%)$) present a deviation.

We proceed as in the previous case, and we first split the two datasets (VSA3E and VSA3G) into two separate parts corresponding to different observation epochs. We find that the non-Gaussian signal connected with VSA3G is only present in one part of the data, while the one corresponding to VSA3E is absent in both parts. This suggests that at least the non-Gaussian signal found in VSA3G with U_2^2 could be due to systematic effects, because is only present in one part of the data.

Next, we have examined the results using the two different noise estimation schemes. Again, varying the noise estimates within $\pm 5\%$ does not change the results on U_2^2 . However, in this case we find a difference between the two methods for the VSA3E and VSA3G pointings. When using a noise estimation based on the scatter of the visibilities when binning all daily observations, we find that now

VSA3G is compatible with Gaussianity ($U_2^2 = 0.33(43.4\%)$), and VSA3E shows a marginal deviation ($U_2^2 = 3.85(95.0\%)$). These results suggest that the non-Gaussian signal found in this mosaic is in reality produced by residual systematic effects associated with a few visibility points which were left in the analysis. This is confirmed when using the other independent data reduction of these two pointings, where we find that both VSA3E and VSA3G are compatible with Gaussianity.

The detailed analysis in separate bins permits us to isolate the origin of this signal, and exclude the affected visibilities. In both cases, it is connected with one single bin (5 and 11, respectively). Once these few visibilities are removed, all the individual pointings become compatible with Gaussianity in the two versions of the data reduction, and the joint analysis of the three-fields mosaic gives $U_2^2 = 1.85(82.7\%)$.

6.3 Corona Borealis mosaic, extended configuration

The previous analysis of the VSA data shows that the STGOF tests are very sensitive methods to detect residual systematic effects in the data and/or deviations of the power spectrum from the average one. To further check the power of this method, we have also applied it to the analysis of the data from a survey in the Corona Borealis supercluster region with the VSA (Génova-Santos et al. 2005). These data are known to present a strong deviation from Gaussianity, associated to a negative decrement in the map which can not be explained in terms of primordial CMB fluctuations, or associated to a (known) cluster of galaxies in the region. A power spectrum analysis of these data presents a clear deviation with respect to the cosmological one in angular scales around $\ell \approx 500$, which corresponds to the angular size of that negative decrement.

Here, we will complete the Gaussianity studies described in Génova-Santos et al. (2005) by performing the simultaneous analysis of the data with the STGOF. We have analysed the 9 pointings which altogether make a mosaic of the central region of the supercluster. Those pointings are noted with letters A,B,C,D,E,H,I,J and K. Given the large size of the full covariance matrix for this dataset ($N_d = 13258$), only the Lanczos method was applied. As shown above, for the signal-to-noise ratios achieved in the VSA observations, the Lanczos method with $m = 1000$, when applied to covariance matrices with $N_d \sim 7000$, gives the same values of the U_i^2 as those obtained with the full analysis if we restrict ourselves to $E_{cut} \gtrsim 0.01$ (i.e. 77 % of the 1000 eigenvalues are good approximations to the true values). In the Corona Borealis case, only ~ 330 eigenvalues are found to be above the cut $E_{cut} = 0.4$, so the use of the Lanczos algorithm is justified.

In the last row of Table 7 we present the results obtained with the Arnoldi algorithm considering $m = 1000$ and $E_{cut} = 0.4$. These numbers show a deviation of the U_2^2 statistic, as we would expect from the fact that the power spectrum of this mosaic differs from the average one.

We now proceed as in the previous cases, and we first analyse all the individual pointings which participate in the mosaic. Considered as a whole, each one of the 9 pointings seem to be consistent with Gaussianity, although the highest U_2^2 value is found for the H pointing ($U_2^2 = 3.72(94.6\%)$)

which contains the main decrement near its centre. However, a detailed analysis in separate bins of all the nine datasets shows that the H pointing is the only one presenting a strong deviation for U_2^2 , and which is associated with the multipole region around $\ell \approx 500$, as we would expect. These results are stable when splitting the data in two separate parts, so the non-Gaussianity seems to be intrinsic to the data. The results are also the same for the two noise estimation schemes.

Finally, we have re-analysed the whole Corona-Borealis mosaic using its own power spectrum, in order to probe if the detected non-Gaussianity is only associated to the fact that we have a deviation of the power spectrum. In this case, we obtain that $U_2^2 = 7.44(99.4\%)$. This result is very interesting, because it is showing that in this case, the non-Gaussianity found in the Corona-Borealis mosaic is intrinsic, and is not associated to a deviation of the power spectrum: even when we use the correct (local) power spectrum of the region in the analysis, the U_2^2 is still showing a detection of a non-Gaussianity.

7 DISCUSSION AND CONCLUSIONS

We have analysed the full VSA data sets presented in Taylor et al. (2003), Grainge et al. (2003), Dickinson et al. (2004) and Génova-Santos et al. (2005), using the Smooth Tests of Goodness-of-Fit adapted to interferometer experiments. This method was described in A05, but here it has been extended to deal with large mosaics via the Arnoldi method. This numerical method permits to solve large eigenvalue problems by reducing the dimensionality of the covariance matrix. We have shown that one implementation of this method for Hermitian matrices, the Lanczos algorithm, is able to provide good approximations to those eigenvalues and eigenmodes of the full covariance matrix with larger signal-to-noise ratio.

From our analysis of the VSA data dedicated to cosmological studies, we found that out of the 13 mosaics presented in Table 7, eleven of them are consistent with Gaussianity, and two of them show a deviation from Gaussianity. In one case (mosaic VSA3E + VSA3F + VSA3G) the non-Gaussian signal is shown to be produced by few visibility points which contain systematic effects that were not removed properly from the data. Once this data are removed, the mosaic becomes compatible with Gaussianity.

In the second case (mosaic VSA2E + VSA2F + VSA2G), we show that the method is detecting a local deviation of the power spectrum with respect to the average one. The STGOF are very sensitive to the power spectrum adopted for the computation of the signal-to-noise eigenmodes, so small deviations from the correct power spectrum are easily detected in the analysis. This ability of the method could be used to study the isotropy of a given CMB map. Moreover, when the data of this mosaic are analysed with their (local) power spectrum, then they are compatible with Gaussianity; but when we analyse the whole data set with the local power spectrum of the VSA2EFG mosaic, then the rest of the mosaics become incompatible with Gaussianity. These results could indicate the presence of anisotropy.

However, there could be other possible explanations, such as the presence of residual foregrounds in this partic-

ular mosaic. Nevertheless, there are no significant features seen in multi-frequency foregrounds maps (408 MHz, H α , 100 μ m dust map) that align with the main features of the VSA mosaic. Moreover, this mosaic is one of the cleanest regions (in terms of rms), as shown in Taylor et al. (2003). Regarding the case of point sources, we have investigated the possibility that this deviation could be produced by two unsubtracted sources with fluxes around 40 mJy. Note that a population of unresolved sources is not a possible explanation, because its contribution should scale as ℓ^2 and it would produce deviations on smaller scales as well. However, two sources would produce structure as a function of ℓ . The value of 40 mJy is an extrapolation to 33 GHz of the completeness limit of the Ryle telescope survey at 15 GHz (see Waldram et al. (2003), and also Cleary et al. (2004) for the details of the survey). The 5-sigma limit from Ryle Telescope at 15 GHz is 10 mJy; the worst case that we can have is a rising spectrum source with index of 2, so we considered the case of two 40 mJy sources. Using Monte-Carlo simulations to explore all the possible relative spatial distributions of the two sources, we find that we can not explain the measured value for U_2^2 in the VSA2G.

It is also interesting to mention that the VSA2F and VSA2G fields are practically contained within the VSA2 mosaic obtained with the compact array. Although those data were obtained with a different configuration, the scales where we find a deviation with the extended array were also sampled with the compact array (but with poorer signal-to-noise ratio), so we could expect a small signature in the analysis. However, the value for VSA2 compact is $U_2^2 = 2.43(88.1\%)$, which is somewhat high but still compatible with Gaussianity.

We also note that the VSA2 and VSA3 fields were already analysed with other Gaussianity tools in Savage et al. (2004) and Smith et al. (2004), but no evidence of non-Gaussian signals was found. This shows the importance of applying a wide number of Gaussianity tests to the data, given that each particular test is sensitive to a different type of non-Gaussianity.

The fraction of data affected by the systematic effects in VSA3 extended I mosaic is too small to affect the published power spectrum by the VSA collaboration. A re-evaluation of the complete VSA power spectrum when we use the corrected version for these data shows no differences with the published values (within the numerical precision of the maximum likelihood code). However, the deviation in the VSA2 extended I mosaic could influence these numbers. Although there is no justified reason to exclude this VSA2 mosaic from the final computation, we have quantified the effect of excluding those data from the final analysis. Thus, we have considered the extreme case in which we remove from the dataset all visibilities which lie inside one of the bins showing the non-Gaussianity. With this new dataset, we have re-evaluated the complete power spectrum, and compared it to the one presented in Dickinson et al. (2004) in order to obtain the maximum deviations that we would expect. Differences (within the numerical precision of the power spectrum code) are only found in three bins (10, 11 & 12), and are of the order of -9.2% , -4.0% and $+4.7\%$ with respect to the published values. To complete this check, we have repeated the parameter estimation analysis described in Rebolo et al. (2004), but now using this new

power spectrum. We have considered two different models, corresponding to use VSA+WMAP data on one hand, and VSA+COBE data on the other hand, and we have explored the 6-parameter flat Λ CDM model described in Table 2 of Rebolo et al. (2004). The differences in all parameters for the VSA+WMAP case are found to be at the most 2%, so we can conclude that the cosmological analyses based on the published data are not affected. However, when using only the VSA+COBE data, we find only a significant difference in the estimate of the baryon density, which turns out to be $\Omega_b h^2 = 0.030^{+0.007}_{-0.005}$ at 68% C.L., and which should be compared with the former value $\Omega_b h^2 = 0.033^{+0.007}_{-0.007}$. This change can be easily understood, because the new power spectrum has less power in the region of the third acoustic peak, giving a smaller (but compatible) value of the baryon density. Note that the new value is now closer to the BBN result, as well as to the result of the analysis using WMAP+VSA.

Finally, we have applied the method to VSA observations of the Corona Borealis supercluster. These observations are known to present a deviation on the power spectrum produced by a strong decrement in one of the pointings (see Génova-Santos et al. (2005)). Our method is able to detect this deviation, and it finds a large value for the U_2^2 statistic which can not be interpreted as systematic effects. A careful analysis shows that the non-Gaussian signal is associated with the same scales where we find a deviation on the local power spectrum, and which correspond to the angular scale of the negative decrement. However, in this case the non-Gaussian signal detected by the method is intrinsic to the data, in the sense that if we use the local power spectrum and we repeat the analysis, a non-Gaussian detection is still present.

ACKNOWLEDGMENTS

We thank the staff of the Mullard Radio Astronomy Observatory, the Jodrell Bank Observatory and the Teide Observatory for invaluable assistance in the commissioning and operation of the VSA. The VSA is supported by PPARC and the IAC. Partial financial support was provided by the Spanish Ministry of Science and Technology project AYA2001-1657. We also acknowledge the Spanish project ESP2004-07067-C03-01.

REFERENCES

- Aliaga, A. M., Rubiño-Martín, J. A., Martínez-González, E., Barreiro, R. B., & Sanz, J. L. 2005, MNRAS, 356, 1559 (A05)
- Aliaga, A. M. 2005, PhD Thesis, Univ. of Cantabria.
- Banday, A. J., Zaroubi, S., & Górski, K. M. 2000, ApJ, 533, 575
- Bartolo, N., Komatsu, E., Matarrese, S., & Riotto, A. 2004, Phys. Rep., 402, 103
- Bennett, C. L., et al. 2003, ApJS, 148, 1
- Bond, J. R. 1995, Phys. Rev. Lett., 74, 4369
- Chiang, L., Naselsky, P. D., Verkhodanov, O. V. & Way, M. J. 2003, ApJ, 590, L65
- Cleary, K. et al. 2004, MNRAS, 360, 340

- Cruz, M., Martínez-González, E., Vielva, P., & Cayón, L. 2005, MNRAS, 356, 29
- Dickinson, C. et al. 2004, MNRAS, 353, 732
- Eriksen, H. K., Hansen, F. K., Banday, A. J., Górski, K. M., & Lilje, P. B. 2004a, ApJ, 604, 14
- Eriksen, H. K., Novikov, D. I., Lilje, P. B., Banday, A. J., & Górski, K. M. 2004b, ApJ, 612, 64
- Génova-Santos et al. 2005, MNRAS, 363, 79.
- González-Nuevo, J., Toffolatti, L., & Argüeso, F. 2005, ApJ, 621, 1
- Grainge, K. et al. 2003, MNRAS, 341, L23
- Hobson, M. P. & Maisinger, K. 2002, MNRAS, 334, 569
- Komatsu, E. et al. 2003, ApJS, 148, 119
- Lancaster, K., et al. 2005, MNRAS, 359, 16
- Mather, J. C., et al. 1994, ApJ, 420, 439
- Park, C. 2004, MNRAS, 349, 313
- Rayner, J. C. W. & Best D. J. 1989, Smooth Tests of Goodness of Fit (New York: Oxford University Press)
- Rebolo, R. et al. 2004, MNRAS, 353, 747.
- Rubiño-Martín, J. A. et al. 2003, MNRAS, 341, 1084
- Saad, Y. 1992, Numerical Methods for Large Eigenvalue Problems (Manchester University Press, <http://www-users.cs.umn.edu/~saad/books.html>)
- Savage, R. et al. 2004, MNRAS, 349, 973.
- Scott, P. F. et al. 2003, MNRAS, 341, 1076
- Slosar, A. et al. 2003, MNRAS, 341, L29
- Smith, S. et al. 2004, MNRAS, 352, 887.
- Taylor, A. C. et al. 2003, MNRAS, 341, 1066
- Vielva, P., Martínez-González, E., Barreiro, R. B., Sanz, J. L., & Cayón, L. 2004, ApJ, 609, 22
- Waldram, E. M., Pooley, G. G., Grainge, K. J. B., Jones, M. E., Saunders, R. D. E., Scott, P. F., & Taylor, A. C. 2003, MNRAS, 342, 915
- Watson, R. A. et al. 2003, MNRAS, 341, 1057